

New results on thermal and photodesorption of CO ice using the novel InterStellar Astrochemistry Chamber (ISAC)

G. M. Muñoz Caro¹, A. Jiménez-Escobar¹, J. Á. Martín-Gago^{1,2}, C. Rogero¹,
C. Atienza³, S. Puertas⁴, J. M. Sobrado¹, and J. Torres-Redondo¹

¹ Centro de Astrobiología (CSIC-INTA), Ctra. de Ajalvir, km 4, Torrejón de Ardoz, 28850 Madrid, Spain
e-mail: munozcg@inta.es

² Instituto de Ciencia de Materiales de Madrid (CSIC), 28049 Cantoblanco, Madrid, Spain

³ Tecnovac S.L., 28760 Tres Cantos, Madrid, Spain

⁴ Maques S.L., C/ Fresadores 8, Polígono Industrial Alcamar, 28816 Camarma de Esteruelas, Madrid, Spain

Received 11 May 2009 / Accepted 2 August 2010

ABSTRACT

Aims. We present the novel InterStellar Astrochemistry Chamber (ISAC), designed for studying solids (ice mantles, organics, and silicates) in interstellar and circumstellar environments: characterizing their physico-chemical properties and monitoring their evolution as caused by (i) vacuum-UV irradiation; (ii) cosmic ray irradiation; and (iii) thermal processing. Experimental study of thermal and photodesorption of the CO ice reported here simulates the freeze-out and desorption of CO on grains, providing new information on these processes.

Methods. ISAC is an UHV set-up, with base pressure down to $P = 2.5 \times 10^{-11}$ mbar, where an ice layer is deposited at 7 K and can be UV-irradiated. The evolution of the solid sample was monitored by in situ transmittance FTIR spectroscopy, while the volatile species were monitored by QMS.

Results. The UHV conditions of ISAC allow experiments under extremely clean conditions. Transmittance FTIR spectroscopy coupled to QMS proved to be ideal for in situ monitoring of ice processes that include radiation and thermal annealing. Thermal desorption of CO starting at 15 K, induced by the release of H₂ from the CO ice, was observed. We measured the photodesorption yield of CO ice per incident photon at 7, 8, and 15 K, respectively yielding $6.4 \pm 0.5 \times 10^{-2}$, $5.4 \pm 0.5 \times 10^{-2}$, and $3.5 \pm 0.5 \times 10^{-2}$ CO molecules photon⁻¹ (7.3–10.5 eV)⁻¹. Our value of the photodesorption yield of CO ice at 15 K is about one order of magnitude higher than the previous estimate. We confirmed that the photodesorption yield is constant during irradiation and independent of the ice thickness. Only below ~5 monolayers ice thickness the photodesorption rate decreases, which suggests that only the UV photons absorbed in the top 5 monolayers led to photodesorption. The measured CO photodesorption quantum yield at 7 K per absorbed photon in the top 5 monolayers is 3.4 molecules photon⁻¹.

Conclusions. Experimental values were used as input for a simple model of a quiescent cloud interior. Photodesorption seems to explain the observations of CO in the gas phase for densities below $3\text{--}7 \times 10^4$ cm⁻³. For the same density of a cloud, 3×10^4 cm⁻³, thermal desorption of CO is not triggered until $T = 14.5$ K. This has important implications for CO ice mantle build up in dark clouds.

Key words. ISM: clouds – ISM: molecules – molecular processes – methods: laboratory – infrared: ISM – techniques: spectroscopic

1. Introduction

Dense molecular clouds in the ISM (typical densities of $10^4\text{--}10^6$ particles cm⁻³) have temperatures as low as 10 K in the interior owing to shielding from UV irradiation. This allows dust particles to accrete ice mantles, with estimated thicknesses of hundredths of a micron. Ice mantles are composed mainly of H₂O and of other species such as CO, CH₃OH, CO₂, and NH₃ (e.g. Gibb et al. 2001). Icy dust particles in the interiors of dense clouds are submitted to energetic processing, mainly by the cosmic-ray induced UV field and partly by direct energy input from cosmic-ray particles. Young stars are born in dense clouds, and the envelopes around stars contain icy grain mantles similar in composition to those present in dense clouds (Thi et al. 2002; Pontoppidan et al. 2005). Such circumstellar ices will be exposed to irradiation from the central star and the surrounding diffuse ISM, providing a new scenario for energetic ice processing (e.g. Muñoz Caro & Schutte 2003). These envelopes often give rise to disks, which in turn can lead to planetary systems.

We present here the novel InterStellar Astrochemistry Chamber (ISAC), designed for studying solids (ice mantles, organics, and silicates) in interstellar and circumstellar environments. It is used to characterize their physico-chemical properties and monitor their evolution as caused by (i) vacuum-UV irradiation; (ii) cosmic ray irradiation; and (iii) thermal processing. To test the capabilities of ISAC, we performed experiments that simulate thermal and photodesorption of CO ice on dust grains, providing new information on these processes.

The first laboratory dedicated to the simulation of energetic processing of interstellar dust was founded in the Leiden Observatory by J. Mayo Greenberg and Lou J. Allamandola in the mid-seventies. The typical experimental system consists of a high vacuum chamber with a pressure on the order of 10^{-7} mbar, where an ice layer is formed at 10 K, which can be irradiated with vacuum UV light or ions.

ISAC is an UHV chamber, with pressure typically in the range $P = 2.5\text{--}4.0 \times 10^{-11}$ mbar. There, an ice layer is made by depositing a gas mixture onto a cold finger from a closed-cycle helium cryostat and can be UV-irradiated. Samples can be heated

from 7 K to 400 K. The evolution of the solid sample is monitored by in situ transmittance FTIR spectroscopy, while the volatile species are monitored by quadrupole mass spectroscopy (QMS). Gas mixtures typically contain H₂O and CH₃OH vapors, mixed with gases like CO, CO₂, and CH₄. The gas line works dynamically, and allows deposition of gas mixtures with the desired composition, and is monitored in real time by QMS. There is a second deposition tube for co-depositing corrosive gases like NH₃. A prechamber is used to extract the samples, thereby preserving the UHV in the main chamber.

Probably the outstanding characteristics of ISAC, compared to other systems, are (i) the excellent UHV conditions with pressures down to 2.5×10^{-11} mbar after baking the system; (ii) the prechamber for extracting samples with no need to break the UHV of the main chamber; and (iii) the novel design of the gas line system for preparing complex gas mixtures with unprecedented accuracy in the composition. In addition to FTIR spectroscopy and QMS, we plan to perform vacuum UV and Raman spectroscopy in the near future and to incorporate an ion source for simultaneous irradiation of the ice with photons and ions.

The density on the surface of the Earth at sea level is the Loschmidt's number, 2.687×10^{19} particles cm⁻³ at 273 K and 1013 mbar. Thus, at room temperature, a rough estimate of the pressure in the dense interstellar medium with densities of 10^3 – 10^6 particles cm⁻³ is between 10^{-14} and 10^{-10} mbar.

Experiments that involve long deposition and simultaneous irradiation times of about one day, using a high deposition flow to form thick ices of more than 1 μm and thus achieve enough products for detailed chemical analysis, are difficult to reconcile with the preservation of UHV conditions, while they can be routinely performed with HV set-ups. On the other hand, when compared to a typical HV set-up, ISAC offers clear advantages inherent to UHV systems: a base pressure below 4.0×10^{-11} mbar corresponds to a particle density that falls within the dense cloud values provided above, and reduces contamination and background accretion onto the cold substrate used for ice deposition. Ice accretion at a deposition rate about 1000 times lower than conventional high vacuum systems can be attained with ISAC. This allows one to work with extremely thin ice films corresponding to one monolayer (abbreviated 1 ML). This is illustrated with the results from our experiments on thermal and photodesorption of CO ice.

The accretion and desorption processes of gas molecules on cold grains play a large role in the evolution of dense clouds and circumstellar regions around YSOs, see e.g. Bisschop et al. (2005) for an introduction. Laboratory simulations of these processes under astrophysically relevant conditions are required to understand them. In particular, that the CO molecule is the second most abundant after H₂ deserves extra attention. Numerous publications were dedicated to studying solid CO in the laboratory (Sandford & Allamandola 1988; Sandford et al. 1988; Kouchi 1990; Palumbo & Strazzulla 1993; Gerakines et al. 1996; Collings et al. 2004; Loeffler et al. 2005; Bisschop et al. 2006; Dartois 2006; Palumbo et al. 2006; Acharyya et al. 2007; etc.). In particular, recent experiments performed under UHV conditions have shown that CO photodesorption can be an efficient desorption mechanism in quiescent dense cloud interiors (Öberg et al. 2007, 2009).

This paper describes the ISAC set-up in Sect. 2 and the experimental protocol in Sect. 3. Section 4 describes the numerical simulations of the thermal gradient at the tip of the cold finger. Section 5 reports the data obtained during the testing of ISAC and the study of thermal desorption of CO ice. Section 6 reports the experimental study of CO ice photodesorption. Section 7 are

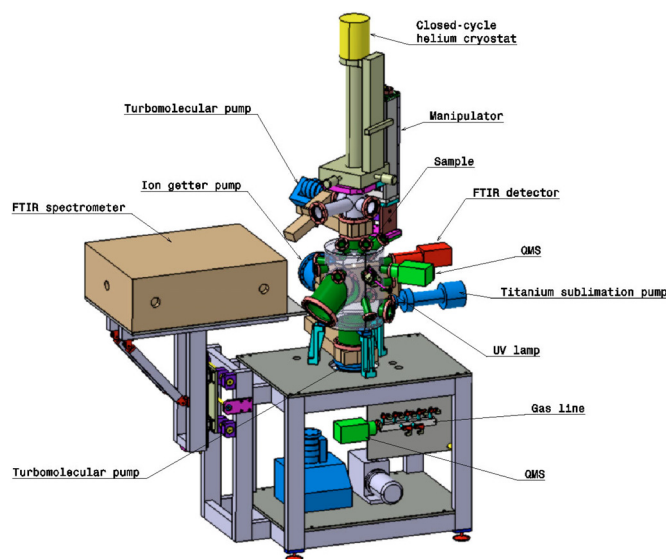


Fig. 1. Schematic cartoon of the ISAC experimental set-up.

the astrophysical implications. The conclusions are summarized in Sect. 8. Appendix A describes the determination of the UV lamp flux. Appendix B provides the calculation of the UV absorption cross section of solid CO.

2. Technical description of ISAC

A cartoon image of ISAC is shown in Fig. 1. The set-up has a vertical configuration, consisting of two chambers: the main chamber, where gas deposition onto a substrate located at the tip of a cold finger from a closed-cycle helium cryostat and irradiation of the formed ice layer takes place, and a prechamber separated by a valve from the main chamber. The prechamber allows the introduction or extraction of samples by lifting up the cryostat, with no need to break the vacuum in the main chamber. The main chamber has two levels. The sample holder with the substrate, usually an infrared transparent window placed at the cold finger is on the upper level, where it is intersected by the beam of the FTIR spectrometer and irradiated by the UV lamp (an ion source and a UV-spectrophotometer will be implemented in the future). There is also a QMS on the upper level for monitoring of the volatiles. A schematic view of the upper level is shown in Fig. 2, with the sample holder at the deposition position. Rotation of the sample holder by 90° is required for FTIR spectrometry of the sample. The lower level is where the pumps are located, the pressuremeters and the Raman spectrometer. As mentioned above, the base pressure at room temperature in the main chamber is 2.5 – 4×10^{-11} mbar, thanks to the combination of a series of UHV pumps. The samples can be cooled down to 7 K and warmed up to 400 K using a closed-cycle helium cryostat and a tunable heater, which in combination with the QMS of the main chamber, allows temperature-programed desorption (TPD) experiments of ices.

A gas line monitored by a second QMS is attached to the main chamber for controlled deposition through the deposition tubes. The gas line consists of a novel design that allows preparation of gas mixtures containing up to 5 different species. The ISAC set-up components are described in more detail below.

- *Prechamber for sample introduction:* A small chamber is on top of the main chamber separated by a hydraulic VAT valve. The samples are introduced and extracted from the

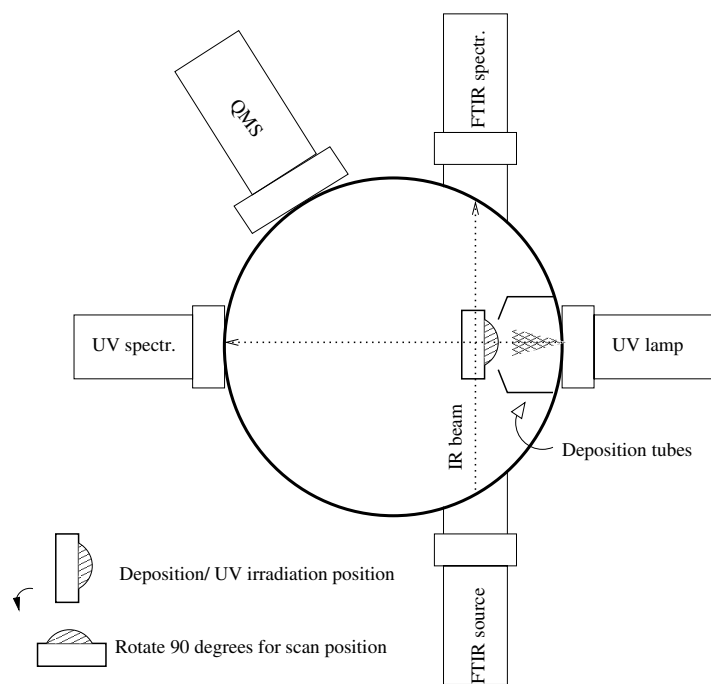


Fig. 2. Schematic representation of the upper level of the main chamber of the ISAC experimental set-up, where gas deposition onto the cold substrate forms an ice layer that is UV irradiated. FTIR and QMS techniques allow in situ monitoring of the solid and gas phases.

set-up via the prechamber with no need to break the UHV in the main chamber. This is done by vertical translational movement of the cold finger, where the sample holder is located. It consists of

- fast entry lock;
- pumping system: independent of the main chamber’s system. It reaches a pressure of about 10^{-9} mbar. It supports the pumping system of the main chamber when the valve connecting the two chambers is open. It consists of a turbomolecular pump (abbreviated TMP) with a pumping capacity of 220 l s^{-1} backed up by a rotary pump and a titanium sublimation pump (TSP);
- cold finger with sample holder connected to a closed-cycle-He-cryostat by a gold ring. The sample holder is mounted on a tube that can be rotated by 360° and moved translationally to place samples in the main chamber. The temperature range is between 7 K and 400 K in the sample position. The sample holder is covered by a radiation shield, sketched in Fig. 3, for thermal isolation. The radiation shield has two holes of $\sim 2.5 \times 3.5 \text{ cm}$ size to allow FTIR spectroscopy in transmittance.
- *Main chamber*: where ice deposition and irradiation takes place. The interior of the chamber is covered by Mu-metal in order to isolate it from external magnetic fields. The UV lamp is positioned in front of the deposition substrate so that the sample is irradiated homogeneously. A cylindrical quartz tube of 10 mm diameter, placed between the lamp and the sample holder, acts as an optical guide to maximize the flux, given in UV photons $\text{cm}^{-2} \text{ s}^{-1}$, at the sample position. A UV spectrophotometer will be mounted on the opposite side of the main chamber to allow in situ monitoring of the UV flux. A Bayer-Alpert pressuremeter measures pressures in

the 10^{-11} mbar range. The characteristics of the deposition or main chamber are

- *Pumping system*: the combination of a series of UHV pumps aims at obtaining a base pressure down to 2.5×10^{-11} mbar. It consists of
 - TMP with a pumping capacity of 550 l s^{-1} . The pump is backed up by a second TMP and a rotary pump;
 - TSP;
 - non-evaporable ion Getter Pump (IGP).
- *Vacuum UV lamp*: the UV source is a microwave-stimulated hydrogen flow discharge lamp (output 1.5×10^{15} photons s^{-1} , $E_{\text{photon}} = 7.3\text{--}10.5 \text{ eV}$), purchased from Opthos, which is separated from the vacuum chamber by an MgF_2 window. Using the x - y manipulator, the sample holder can be positioned in close contact to a quartz tube that acts as a light guide. That way, the circular spot size of the UV flux at the sample position has a slightly larger diameter than the 10 mm diameter of the quartz tube, which roughly corresponds to the size of the 13 mm diameter infrared transparent window where ice deposition takes place. The UV lamp requires a simple circuit where hydrogen circulates from a hydrogen bottle to the lamp and is pumped by a roughing pump. The working pressure in our experiments is 0.4–0.6 mbar. A microwave generator with 100 W power is used to excite the hydrogen. The Evenson cavity of the lamp is refrigerated with air. The UV photon spectrum of this hydrogen-lamp resembles that of the diffuse interstellar UV field (Jenniskens et al. 1993; Muñoz Caro & Schutte 2003).
- *Analytical techniques*: provide in situ characterization of the samples during the deposition/irradiation and warmup. Fourier-transform infrared (FTIR) spectroscopy monitors the ice composition and aids characterization of the more refractory products observed at room temperature. Due to the different selection and excitation rules, Raman spectroscopy allows detection, general characterization, and determination of the structure of organic matter, even at cryogenic temperatures. The quadrupole mass spectrometer (QMS) enables in situ detection of volatiles produced during warmup of the ice and serves to control the gas deposition. A vacuum ultraviolet (VUV) spectrometer will be used to monitor the flux of the UV lamp and to measure the sample absorption in that spectral range.
 - *Transmittance FTIR spectroscopy*: using a Vertex 70 Bruker spectrometer, equipped with a DTGS detector working in the 7500 to 370 cm^{-1} (~ 1.3 to $27 \mu\text{m}$) spectral range. The infrared beam goes across the main chamber through two ZnSe windows.
 - *Raman spectrometry*: a HORIBA Jobin Yvon iHR550 spectrometer. The laser wavelength is 532 nm (green). The incident laser makes an angle of 45° with the deposition window.
 - *Quadrupole mass spectrometry (QMS)*: Pfeiffer Prisma of mass spectral range from 1 to 200 amu with a channeltron detector.
 - *Vacuum UltraViolet (VUV) spectrometry*: model 234/302 McPherson spectrometer with a 658 photomultiplier tube (PMT) detector working in the 30 to 200 nm spectral range.

- *Gas line*: prepares of gas mixtures for deposition. A mixture of a maximum of 5 components can be prepared in the gas line. The design of a gas line for the preparation of a complex gas mixture under controlled conditions, containing H₂O and CH₃OH vapors and three gas components, commonly CO, CO₂, and CH₄, was an important challenge. This was accomplished using electrical valves to control the entrance of the individual components and working dynamically at a total pressure below 1 mbar, thus ensuring laminar flow conditions. The electrical valves are activated according to the partial pressures measured by a QMS (Pfeiffer prisma of mass spectral range 1–100 amu with a Faraday detector), which is connected to the gas line. Either CH₃OH or H₂O is deposited manually into the gas line, and the other components are deposited proportionally to the amount of CH₃OH or H₂O in the gas line. The QMS monitors the composition of the gas mixture at any time. When the desired composition of the gas mixture is obtained, the deposition tube is opened through a needle valve and the gas enters the main system, accreting onto the substrate window at 7 K and forming an ice layer. In addition, there is a second deposition tube for the deposition of corrosive gases like NH₃ into the main chamber.

3. Experimental protocol

The experimental protocol that is described below corresponds to a deposition/irradiation experiment for the simulation of icy grain mantle processing in the interstellar/circumstellar medium. It comprises the following steps:

- In the prechamber compartment, while the valve between the prechamber and the main chamber is closed, an infrared transparent window (CsI or KBr) is fixed on the tip of the cryostat. The infrared window serves as the substrate for the deposition. Afterwards, the fast entry lock is closed and the prechamber is evacuated.
- Once the vacuum in the prechamber is close to 10⁻⁹ mbar, the valve connecting the prechamber to the main chamber is opened. The base pressure in the main chamber should be below 4 × 10⁻¹¹ mbar and the cryostat is moved downwards so that the substrate is at the deposition/irradiation position.
- A gas mixture for deposition is prepared in the gas line. Predeposition is started, with the substrate at room temperature, to calibrate the flow of the deposition and set the valve positions that correspond to the desired gas flow. The Langmuir relation provides an approximation of the number of ML of ice deposited as a function of the gas pressure and the deposition time, assuming a sticking coefficient equal to unity, which is valid for cryogenic temperatures around 10 K. One Langmuir (1 L) corresponds to the deposition of 1 ML and is given by 1 L = 10⁻⁶ Torr s.
- The cryostat is turned on and the temperature reaches 7 K. The valve connecting the gas line with the main chamber is opened at the position determined during the predeposition to start the deposition. During the deposition the ice layer can be irradiated with photons and/or ions. At different intervals, the cryostat can be rotated 90° to perform

transmittance FTIR spectroscopy of the ice. The column density of the deposited ice is calculated according to the formula

$$N = \int_{\text{band}} \frac{\tau_{\nu} d\nu}{A} \quad (1)$$

where N is the column density in cm⁻², τ_{ν} the optical depth of the band, $d\nu$ the wavenumber differential in cm⁻¹, and A the band strength in cm molecule⁻¹. The integrated absorbance is equal to 0.43 × τ , where τ is the integrated optical depth of the band. The adopted band strength for CO was $A(\text{CO}) = 1.1 \times 10^{-17}$ cm molecule⁻¹ (Jiang et al. 1975). Raman spectroscopy can be done at the deposition/irradiation position of the sample. QMS monitors the gas phase molecules during the deposition and irradiation.

- Once the deposition/irradiation is completed, the warmup can be started following a linear heating ramp of 1 K min⁻¹ or lower. QMS is used to detect volatiles during warmup, while FTIR and Raman spectroscopy monitor changes in the ice composition and structure.
- At room temperature, the cryostat is pulled up, and the substrate with the refractory organic residue is now in the prechamber, which is isolated from the main chamber closing the VAT valve, so that the sample can be extracted from the set-up without breaking the vacuum in the main chamber. The organic residue, obtained from irradiation and warmup of the interstellar/circumstellar ice analog, can be analyzed ex situ by other techniques.

4. Numerical simulations of the thermal gradient on the cold finger of ISAC

There are two thermocouples for temperature measurements installed on the cold finger, one measures the lowest temperature achieved by the cryostat, another measures the temperature at the bottom of the sample holder. The lowest temperatures measured by both thermocouples are ~6–7 K and 9 K.

The temperature of the substrate where ices are grown during deposition is a key parameter to determine the ice desorption temperatures and, in general, the temperature of the ice at a given moment. Using the EFD LAB software, we simulated the temperature distribution in the chamber, when the cryostat is on and the temperature on the tip of the cryostat is 6 K. The effect of a copper radiation shield protecting the tip of the cold finger, where the sample holder with the deposition substrate is located, was also simulated. The radiation shield is in contact with the walls of the cold finger at liquid nitrogen temperature. Figure 3 shows the temperature distribution inside the UHV chamber, with no radiation shield (top panel) and when the radiation shield is installed (bottom panel).

In both cases, with and without the radiation shield, the temperature of the deposition substrate is 7 K at the edges and 7.5 K at the center. The distribution of the dark blue color around the sample holder shows that the radiation shield keeps the temperature near 7 K in the vacuum enclosing the deposition substrate. In the real experiment, the thermocouple that measures the temperature is located at the bottom of the sample holder, where the simulated temperature estimate is around 7.0 K. That means that the expected difference between the temperature measured by the thermocouple and the temperature at the deposition substrate

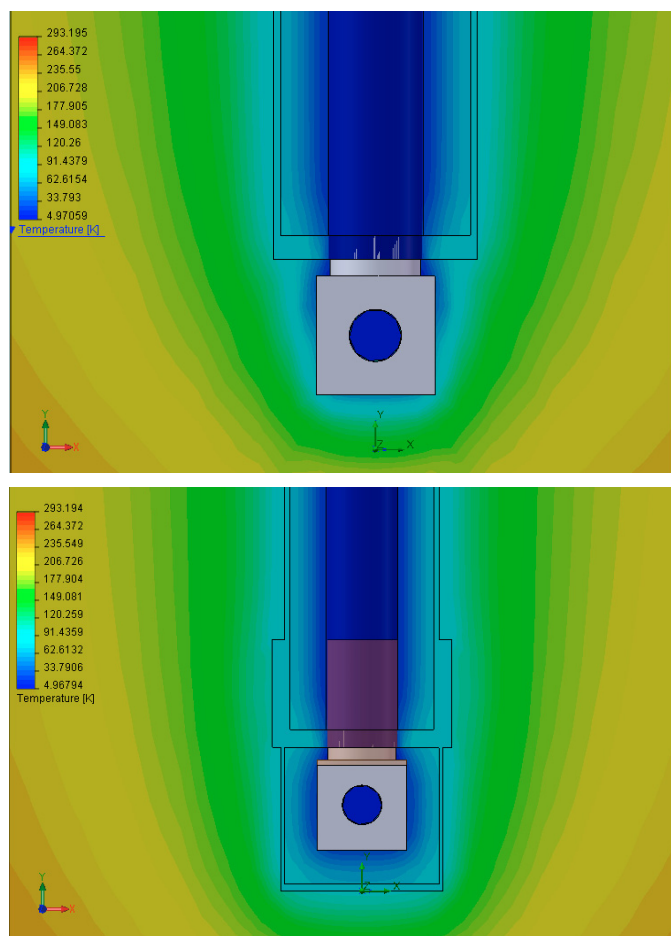


Fig. 3. Simulated temperature gradient distribution inside the UHV chamber without radiation shield (*top panel*) and with a copper radiation shield covering the tip of the cold finger (*bottom panel*).

is no more than 0.5 K. The simulations showed that the temperature in the vacuum enclosing the sample holder increases rapidly even when the radiation shield is installed; e.g., at 0.5 mm, the temperature is above 20 K with radiation shield and above 40 K with no radiation shield. It is therefore important that the thermocouple is in good thermal contact with the sample holder. This rapid increase in temperature also occurs as we move away from the deposition substrate: at 0.1 μm above the substrate the estimated temperature value is about 10 K.

It should be noted that the only cold surfaces where CO gas can accrete are the sample holder and the substrate; see estimated temperatures above. As mentioned above, other cold surfaces, i.e. the radiation shield and the walls of the cold finger, are at liquid nitrogen temperature or above, i.e. $T \geq 77$ K. This temperature is too high to allow CO ice formation. Water ice can form on the radiation shield and the cryostat walls by background water accretion or in water deposition experiments. Background water accretion on the substrate, however, is negligible at base pressures in the 10^{-11} mbar range. Because the deposition tubes are both pointing to the substrate, at a distance of about 3 cm, most molecules impinge on the substrate. We observed that if the cryostat is turned by 90° (scan position, see Fig. 2) the radiation shield prevents accretion on the substrate. During controlled warm-up of the ice in ISAC, only the sample holder and the substrate are heated directly with a resistance. Meanwhile the cryostat remains switched on to prevent desorption from other surfaces. Only when the TPD experiment is complete is the

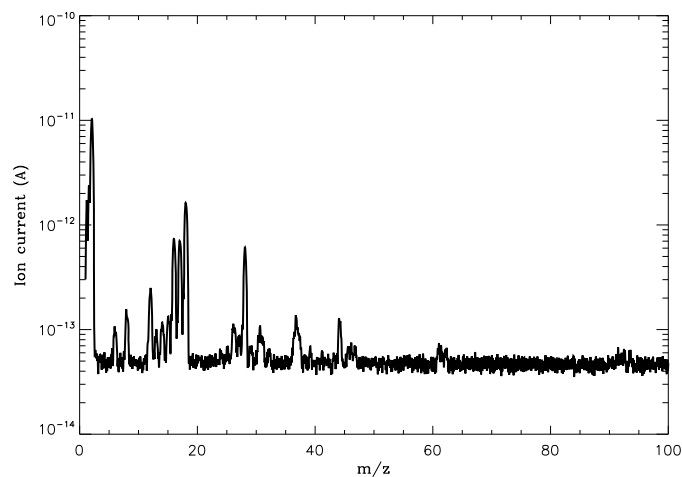


Fig. 4. Residual gas analysis in the main chamber of ISAC. The total gas pressure measured by a Bayer-Alpert gauge was 3.6×10^{-11} mbar. The intensity scale on this plot corresponds approximately to pressure in mbar units. The most abundant species are H_2 ($m/z = 2$), H_2O ($m/z = 18$), CO/N_2 ($m/z = 28$), CH_3OH ($m/z = 31$), and CO_2 ($m/z = 44$). The level of organic contaminants, toluene, or xylene at $m/z = 91$ and 92, is below 10^{-13} mbar.

cryostat switched off, and then desorption of H_2O molecules from the radiation shield and the cryostat walls is observed.

5. Experimental study of the thermal desorption of CO ice. Testing ISAC

Figure 4 shows the mass spectrum of the residual gas in the main chamber of ISAC, measured when the base pressure was 3.6×10^{-11} mbar. Under those UHV conditions, the dominant gas component is H_2 , as seen in the figure caption. A simple test can be carried out to observe the pumping efficiencies of the different pump types by closing one pump at a time and observing the change in the base pressure value inside the main chamber. This is shown in Fig. 5 for the 10^{-11} mbar range. The partial pressures of H_2 , H_2O , and CO/N_2 increase significantly when the valve connecting the IGP to the main chamber is closed, and rapidly reach their initial values when the valve is opened again, showing that those gas components are continuously pumped by the IGP. Only H_2 is clearly pumped continuously by the TSP, albeit less efficiently than the IGP. H_2 , CO/N_2 , Ar, and CH_4 gas molecules are pumped continuously by the TMP. Except for eventual jumps during valve opening/closing, likely due to retained pockets of gas, the partial pressures of CH_3OH , O_2 , and CO_2 do not vary much, indicating that those species have reached their minimum partial pressure values.

The results presented here correspond to the thermal desorption of CO ice. The relative concentrations of the gas components in the gas line are monitored continuously and were found to be very stable even for experiments of long duration, i.e. longer than one day. Figure 6 shows the concentration of gases in the gas line during the CO predeposition at room temperature and the real deposition at 7 K; see Sect. 3 for explanation of the experimental protocol. CO has a concentration above 99%, compared to the residual gases that remain in the gas line. Residual H_2O has a relative abundance below 1%, while those of the CO_2 and CH_3OH remaining in the gas line from a previous experiment are below 0.1%.

The QMS located in the main chamber measures the increase in the partial pressure of CO when predeposition is started. This

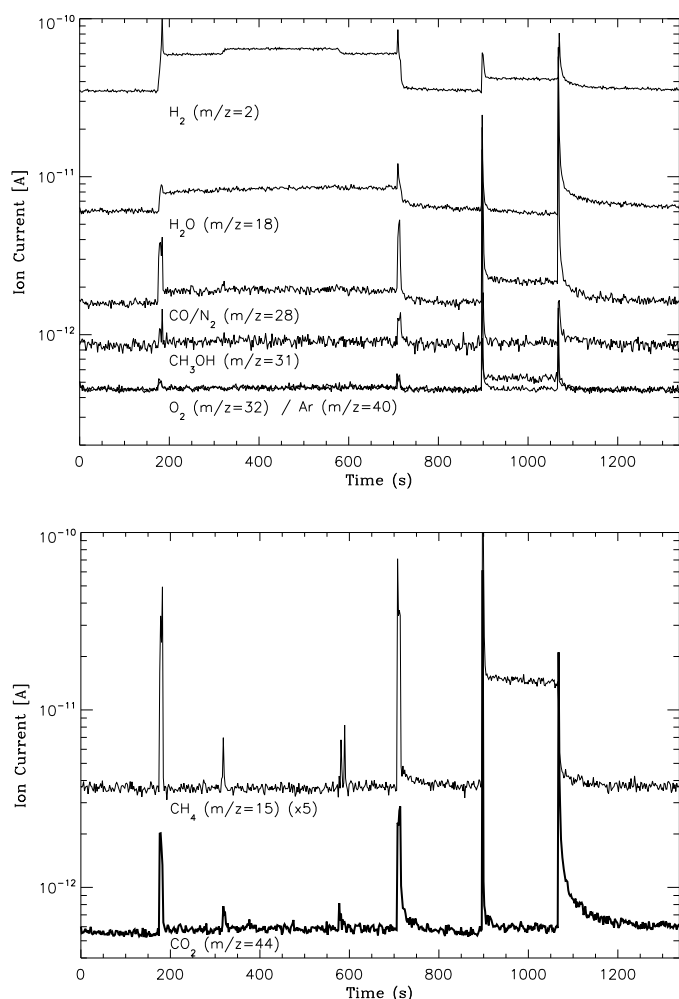


Fig. 5. Evolution of the partial gas pressures is coupled to the operation of the different pumping systems as follows: i) the valve connecting the IGP to the main chamber is closed after 175 s; ii) in addition the TSP valve is closed after 315 s; iii) the TSP valve is opened after 575 s; iv) the IGP valve is opened after 705 s; v) the TMP valve is closed after 895 s; vi) the TMP valve is opened after 1067 s.

is illustrated in Fig. 7. CO is detected for $m/z = 28$. It is found that $m/z = 2, 18, \text{ and } 44$, corresponding to residual H_2 , H_2O , and CO_2 , also increase during the predeposition of CO, but their partial pressures are very low compared to that of the deposited CO.

After 10.8 ML were deposited at 7 K with a deposition rate of $6.2 \times 10^{-3} \text{ ML s}^{-1}$, calculated from integration of the CO ice absorption at 2138 cm^{-1} and Eq. (1), assuming that $1 \times 10^{15} \text{ molecules cm}^{-2}$ is 1 ML coverage, we started the warmup increasing the temperature slowly at 1 K min^{-1} . The QMS detected an increase of CO in the gas phase, reaching a maximum at 28 K, corresponding to the desorption temperature of CO under UHV conditions. This temperature value for the desorption of pure CO ice is in good agreement with the values previously reported (e.g. Acharyya et al. 2007). This is shown in Fig. 8. A slight increase in the partial pressure of H_2 is observed. H_2 is not expected to accrete onto the substrate at 7 K, the substrate temperature during CO deposition, but can be trapped in the micropores of CO ice. As an example, the incorporation of H_2 molecules in microporous water ice at 10 K was reported by Rowland et al. (1991). The small bump from 15 K to 23 K in the desorption curve of CO ice coincides with the H_2 desorption

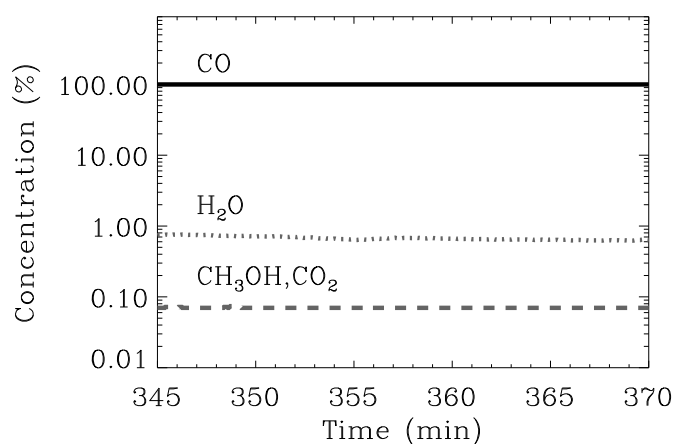


Fig. 6. Relative abundances of CO and the residual gas species present in the gas line during CO pre-deposition at room temperature and during the CO deposition experiment at 7 K. The y -scale is logarithmic.

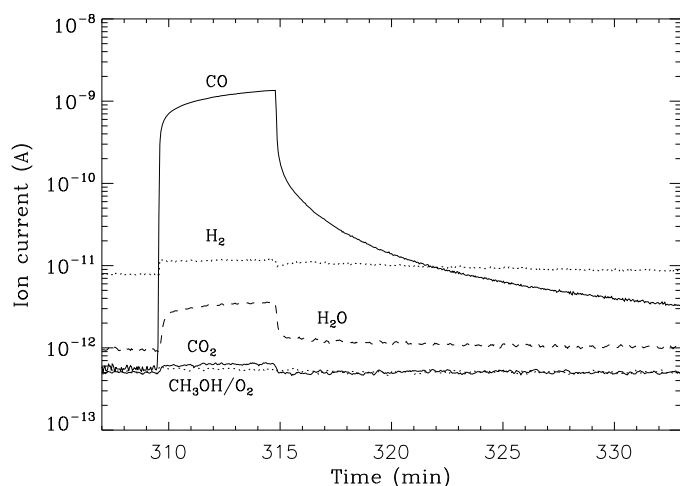


Fig. 7. Partial pressure of CO in the main chamber during predeposition. The ion current in A, represented on the y -scale, corresponds roughly to the partial pressure in mbar. The most abundant residual components remaining in the chamber have $m/z = 2, 18, 44, \text{ and } 32$, and correspond to $\text{H}_2, \text{H}_2\text{O}, \text{CO}_2, \text{ and } \text{CH}_3\text{OH}/\text{O}_2$.

peak, see Fig. 8, suggesting that this early desorption of CO is caused by the release of H_2 molecules from the CO ice.

Figure 9 presents the infrared band corresponding to the stretching mode of CO ice at different temperatures during warmup. Each spectrum corresponds to 128 scans at resolution 4 cm^{-1} . The desorption starting at 15 K, detected by QMS, is not observed in the infrared spectra shown in the top panel of Fig. 9, which is most likely due to the lower sensitivity of our infrared spectrometer compared to the QMS.

Desorption is clearly detected for temperatures above 25 K in the infrared, as a clear decrease in the CO band absorption area, see bottom panel of Fig. 9. The column densities of CO ice at different temperatures, represented as diamonds in Fig. 11, were estimated using Eq. (1).

The TPD spectra of pure CO in Acharyya et al. (2007) and other works do not show the desorption of amorphous CO starting at 14 K, that crystallizes to α -CO at 23 K, according to Kouchi (1990). When the deposition rate is over 100 nm h^{-1} ($8.7 \times 10^{-2} \text{ ML s}^{-1}$), crystalline α -CO condenses even at 10 K

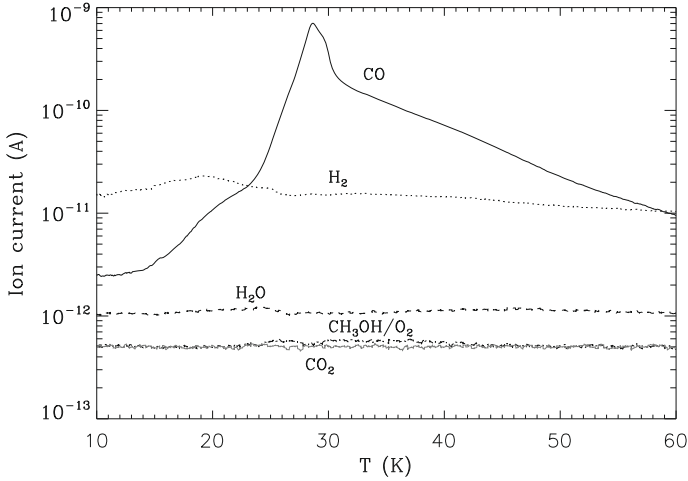


Fig. 8. CO ice desorption during warmup. The main residual gas components are also shown: H₂, H₂O, CH₃OH/O₂, and CO₂. The ion current (A) is plotted on a logarithmic scale for a better appreciation of the curve profile, and corresponds roughly to partial pressure in mbar.

(Kouchi 1990). Following Kouchi (1990), the degree of crystallinity of CO ice, which relates to the desorption of amorphous CO, will therefore depend on the temperature and rate of deposition used in the experiment. As already mentioned, the small bump from 15 K to 23 K in the desorption curve of CO, Fig. 8, is most likely induced by the release of H₂ molecules from the CO ice. Therefore, this early desorption of CO can be explained with no need to invoke the desorption of amorphous CO reported by Kouchi (1990) occurring in a similar temperature range. Similar to the experiments reported by Kouchi (1990) on CO:H₂O ice desorption, to prove the presence of amorphous or crystalline CO ice in our experiments, an analysis technique similar to reflection electron diffraction is required.

We found that a good fit of the TPD curve of CO in our experiments, using the Polanyi-Wigner equation, clearly requires a second exponential term. Indeed, the slope of the TPD curve of CO above 23 K is only well-fitted as the sum of two exponentials. A possible interpretation of the need for a second exponential term is that H₂ release in fact continues up to about 26 K, see Fig. 8, contributing to the desorption of CO up to that temperature. In the astrophysical context of dense cloud interiors, where H₂ is abundant, this desorption of CO is expected to play a role, and therefore including a second term in the Polanyi-Wigner equation is justified. We performed an experiment where CO was deposited at 20 K and cooled down to 8 K. The ice was then warmed-up at a rate of 1 K min⁻¹. The desorption curve of this experiment is shown in Fig. 10. There was no significant H₂ desorption during warm-up below 20 K in this experiment, which suggests that H₂ is not trapped in CO ice when formed at 20 K as much as it is trapped in the 7 K deposition experiment. In this experiment, the bump observed between 15 and 23 K in the desorption curve of CO ice deposited at 7 K is not observed. This provides more evidence that the desorption of CO below 23 K for the 7 K deposition experiment is induced by the release of H₂ from CO ice.

The desorption rate, in molecules cm⁻² s⁻¹, of CO ice is given by the Polanyi-Wigner equation

$$\frac{dN_g(\text{CO})}{dt} = \nu_i [N_s(\text{CO})]^i \exp\left(-\frac{E_d(\text{CO})}{T}\right) \quad (2)$$

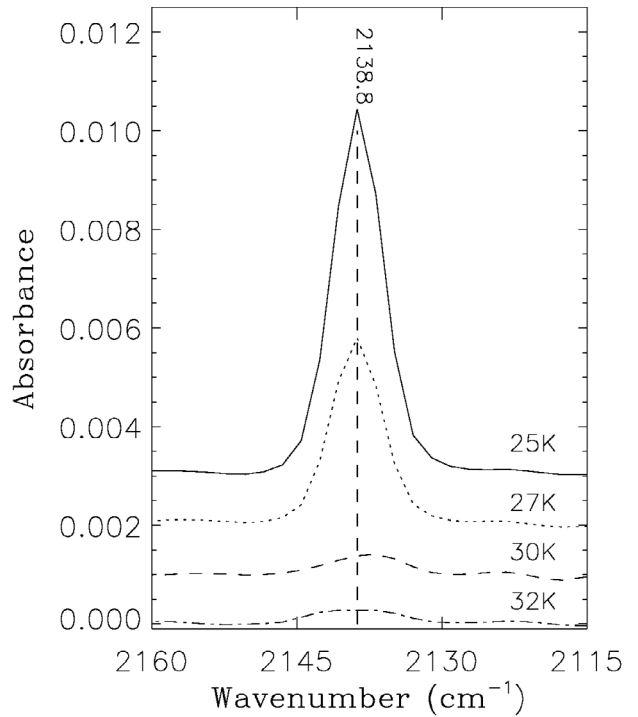
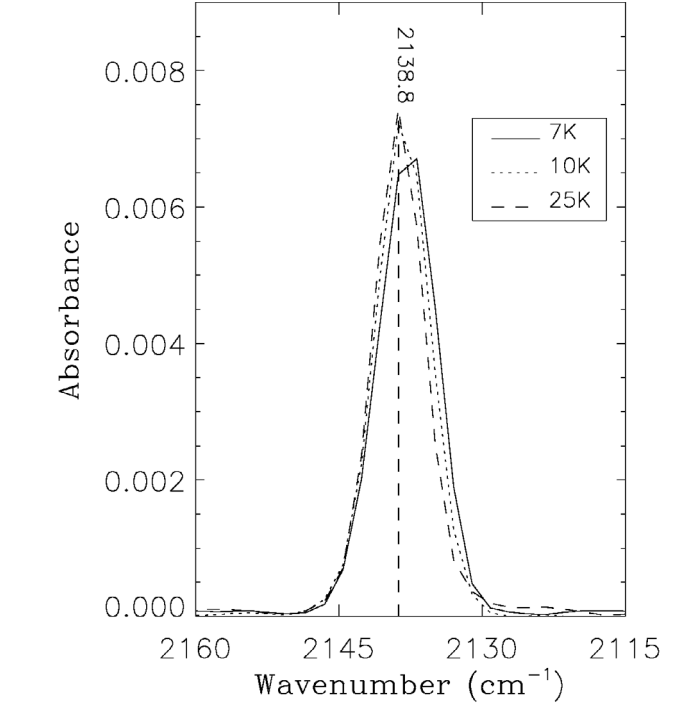


Fig. 9. Infrared band of CO ice at different selected temperatures during warmup.

where $N_g(\text{CO})$ is the column density of CO molecules desorbing from the ice surface (cm⁻²), ν_i a frequency factor (molecules¹⁻ⁱ cm⁻²⁽¹⁻ⁱ⁾ s⁻¹) for desorption order i , $N_s(\text{CO})$ the column density of CO molecules on the surface at time t , $E_d(\text{CO})$ the binding energy in K, and T the surface temperature in K. The TPD data can be fitted using Eq. (2) and the relation

$$\frac{dN_g(\text{CO})}{dt} = \frac{dT}{dt} \frac{dN}{dT} \quad (3)$$

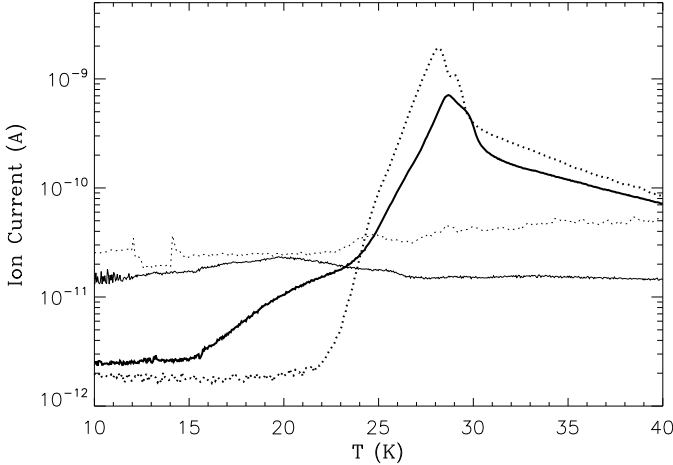


Fig. 10. CO ice desorption during warmup for two different deposition temperatures, 7 K (thick solid trace) and 20 K (thick dotted trace). The desorption of H₂ in the samples deposited at 7 K (thin solid trace) and 20 K (thin dotted trace) are also shown. The ion current (A) is plotted on a logarithmic scale, for a better appreciation of the curve profile, and roughly corresponds to partial pressure in mbar.

where $\frac{dT}{dt}$ is the heating rate, 1 K min⁻¹ in our case. The TPD curve of CO shown in Fig. 8 results from the desorption of CO induced by the release of H₂ trapped in CO and the common CO desorption reported in the literature, each having a different desorption temperature and desorption rate. Other works, e.g. Acharyya et al. (2007), only use one exponential term, but the fit is not as good, see Fig. 4a of that paper. Thus, for zero-order, Eq. (2) can be expressed as

$$\frac{dN_g(\text{CO})}{dt} = \nu_0(\text{H}_2 \text{ ind. CO}) \exp\left(-\frac{E_d(\text{H}_2 \text{ ind. CO})}{T}\right) + \nu_0(\text{CO}) \exp\left(-\frac{E_d(\text{CO})}{T}\right) \quad (4)$$

where $\nu_0(\text{H}_2 \text{ ind. CO})$ and $E_d(\text{H}_2 \text{ ind. CO})$ correspond to the desorption of CO induced by H₂ release, while $\nu_0(\text{CO})$ and $E_d(\text{CO})$ apply to the usual CO desorption. The coverage is given by $N_s(\text{CO})$, and corresponds to the column density of solid CO at the cold substrate. It is obtained from

$$\frac{dN_s(\text{CO})}{dt} = 1 - \frac{dN_g(\text{CO})}{dt}, \quad (5)$$

where $\frac{dN_g(\text{CO})}{dt}$ is derived from Eq. (4). Figure 11 shows that, with the exception of the small bump from 15 to 23 K, Eq. (4) provides an excellent fit of the TPD data using the parameter values $\nu_0(\text{H}_2 \text{ ind. CO}) = 5.1 \times 10^{21}$ molecules cm⁻² s⁻¹ and $E_d(\text{H}_2 \text{ ind. CO}) = 490$ K for the desorption of CO ice induced by H₂ release, and for the usual desorption of CO ice the values $\nu_0(\text{CO}) = 6.5 \times 10^{26}$ molecules cm⁻² s⁻¹ and $E_d(\text{CO}) = 834$ K. Also the coverage datapoints (diamonds), measured by infrared spectroscopy, are very well fitted by Eq. (5). We conclude that there is very good agreement between the coverage curve calculated by fitting the TPD curve measured by QMS (solid gray line), and the coverage values measured by transmittance FTIR (diamonds). Only the last three diamond datapoints are not well fitted. The reason is that by definition a zero-order fit works when there is an unlimited supply of particles, but fails when the coverage is less than 1×10^{15} molecules cm⁻², i.e. 1 ML, as Fig. 11 shows.

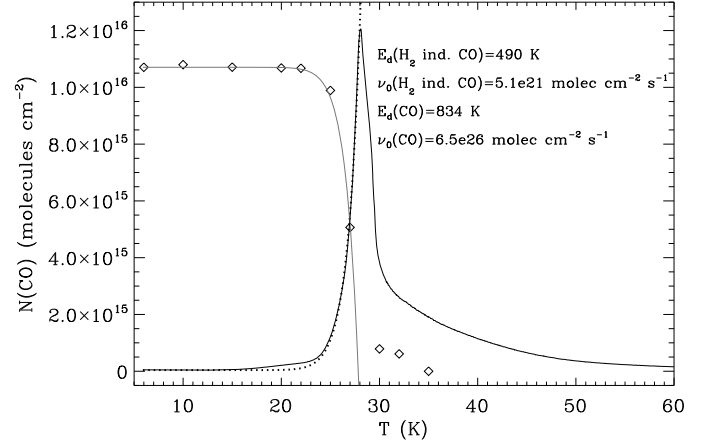


Fig. 11. Data points correspond to the column densities of CO for the different temperatures during warmup. Brought to the same scale is the TPD curve of CO shown in Fig. 8, now on a linear scale. The dotted line is the fit corresponding to the Polanyi-Wigner expression, Eq. (4). The gray line is the calculated zero-order coverage using Eq. (5).

6. Experimental study of the photodesorption of CO ice

The UV photodesorption of CO ice was found to be more efficient than previously thought, a desorption rate of 3×10^{-3} CO molecules per incident photon was measured at 15 K (Öberg et al. 2007). Desorption of CO ice starts around 15 K in our thermal desorption experiments, see Sect. 5, in line with previous works, e.g. Kouchi (1990). Irradiation at a lower temperature is thus desirable to better differentiate thermal and photodesorption.

The reason to carry out the CO photodesorption experiment is twofold: first, to check the reproducibility of the results reported by Öberg et al. (2007) irradiating with the same hydrogen UV lamp they used but at a lower temperature, i.e. 7 K instead of 15 K; and second, because CO ice photodesorption is a good example of a problem that can only be studied properly under UHV conditions, and allows a test of the performance of the ISAC set-up by measuring effects that occur on the ML scale. The accretion of residual gases onto the cold substrate is about 6 ML min⁻¹ for HV set-ups with a base pressure of $\sim 10^{-7}$ mbar, and is dominated by H₂O accretion. As we will see, the thickness of the deposited ice in our CO photodesorption experiment was 15.9 ML, and the observed photodesorption rate of CO ice was ~ 1 ML min⁻¹, i.e. 6 times lower than the deposition of background water in HV set-ups, which clearly demonstrates the need of UHV conditions to perform CO photodesorption experiments.

Section 6.1 presents two thin CO ice experiments, one performed at 7 K with 15.9 ML CO ice thickness and another one performed at 8 K with 12 ML CO ice thickness, to study the photodesorption of the monolayers close to the substrate. Section 6.2 presents the experiments of thick CO ice, >600 ML, photodesorption at 8 K and 15 K, where all photons are absorbed in the ice.

6.1. Photodesorption of thin CO ice at 7 and 8 K

Transmittance FTIR allows better quantitative analysis than other techniques used for infrared spectroscopy of ice, because the column density of an optically thin ice layer can be determined accurately using Eq. (1), as shown in Sect. 5. Figure 12

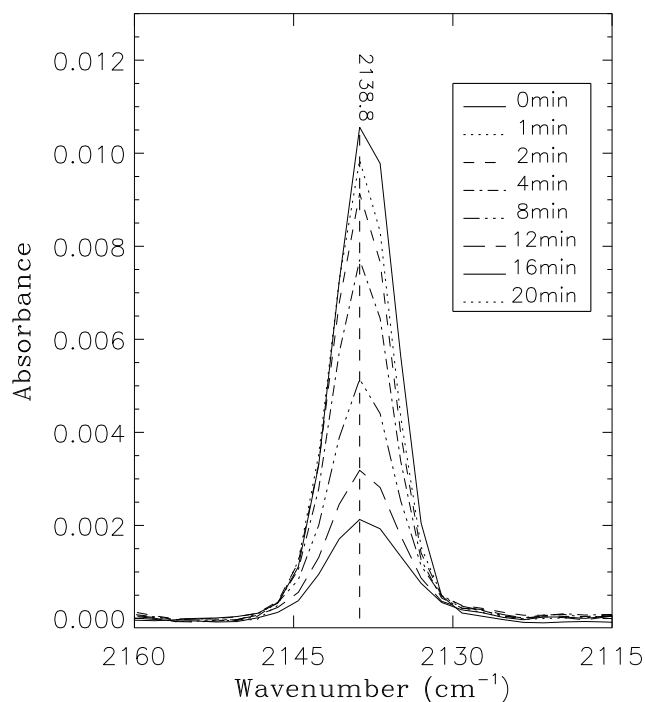


Fig. 12. Evolution of the CO ice band during UV irradiation at 7 K.

shows the decrease in the infrared CO band area for different irradiation times at 7 K; values of the integrated absorbance corresponding to those bands are given in Fig. 13. Also shown in Fig. 13 are the integrated absorbance values corresponding to a similar experiment performed at 8 K. In experiments where CO ice deposition and irradiation was performed at 7 K, about 16 ML were deposited at a rate of $5.4 \times 10^{-2} \text{ ML s}^{-1}$. For similar experiments at 8 K, 12 ML were deposited at the same rate. It is observed that the decrease in the band absorption is linearly proportional to the irradiation time, in agreement with the results from Öberg et al. (2007), but this linearity fails when the value of the integrated absorbance of the CO ice band is below ~ 0.024 , corresponding to about 5 ML, according to Eq. (1) assuming that a surface coverage of $10^{15} \text{ molecules cm}^{-2}$ corresponds to 1 ML. This observation indicates that only the top 5 ML contribute to the photodesorption of CO. This result does not agree with Öberg et al. (2007), who report no decrease in the photodissociation rate even when the CO ice thickness was 1 ML. This issue is discussed below.

Figure 14 shows the detection of gas CO molecules during the photodesorption of CO ice at 7 K, and traces of residual molecules codesorbing with CO. Peaks show a sudden rise corresponding to the start of irradiation, and a fast drop when irradiation is stopped related to the high pumping capacity of ISAC. The different width of the desorption peaks of CO is simply due to the difference in the time interval of irradiation, in order of time appearance: 1, 1, 2, 4, 4, 4, and 4 minutes (see inset of Fig. 12). The height of the peaks in Fig. 14 is more relevant than their width, since it is related to the number of molecules desorbing per unit of time. A decrease in the height of the CO peaks is clearly observed after some time, and coincides with the decrease in the desorption rate inferred from the infrared observations, i.e. when the ice thickness is less than about 5 ML.

A photodiode for the measurement of the UV flux is not operating in our system. The flux value measured by Cottin et al. (2003), Table 1, for the same Opthos lamp and a

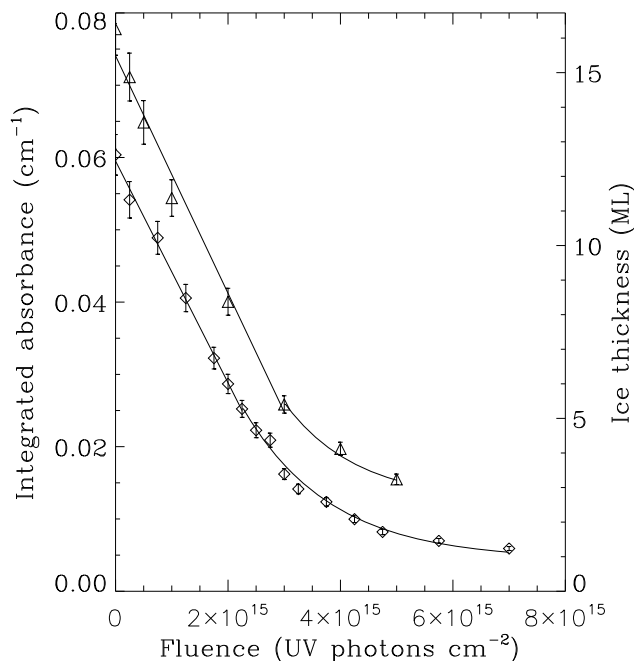


Fig. 13. Decrease in the absorption area (integrated absorbance) of the CO ice band as a function of fluence, see Sect. 3 for the determination of the integrated absorbance. Triangles and diamonds correspond respectively to datapoints for 7 K and 8 K experiments. Roughly, 1 ML of ice is equivalent to a column density of $1 \times 10^{15} \text{ molecules cm}^{-2}$.

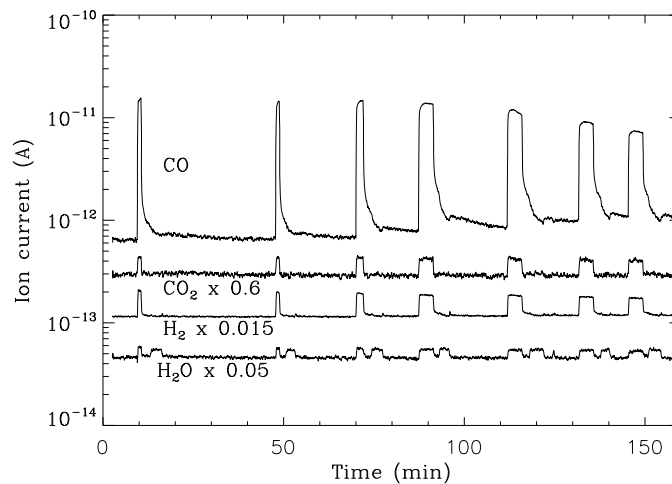


Fig. 14. QMS data measured during the photodesorption of CO at 7 K. Peaks correspond to the desorption of CO and residual molecules during the different irradiation intervals.

forward/reflected power of 70/6, similar to the one used in our experiment, is $4.17 \times 10^{14} \text{ photons cm}^{-2} \text{ s}^{-1}$. However, the H_2 pressure at which they operate the UV lamp is very high: 1000 torr compared to 0.3 torr in our experiments. That difference in hydrogen pressure changes the emission spectrum of the lamp drastically, since high pressure reduces the Lyman- α emission. From the UV lamp emission spectrum (Muñoz Caro & Schutte 2003), the average photon wavelength and energy are, respectively, 135.1 nm and 9.2 eV in our experiments. The output of the lamp measured for an H_2 pressure similar to the one in our experiment, is $1.5 \times 10^{15} \text{ photons s}^{-1}$ (Weber & Greenberg 1985). In our experiment, the distance between the exit of the UV lamp and the deposition substrate is 15 cm. There is an

optical guide consisting of a quartz tube to direct the photons to the sample. Prior to the CO photodesorption study, we performed experiments on the photolysis of O₂ at 7 K under the same conditions, and found that the incident flux at the sample position was 2.5×10^{14} photons cm⁻² s⁻¹, see Appendix A. The photodesorption rates corresponding to the linear fits in Fig. 13 are 1.6×10^{13} CO molecules cm⁻² s⁻¹ at 7 K and 1.3×10^{13} CO molecules cm⁻² s⁻¹ at 8 K. For our estimated flux value of $\sim 2.5 \times 10^{14}$ photons cm⁻² s⁻¹ at the sample position, the photodesorption yield per incident photon at 7 K is $6.4 \pm 0.5 \times 10^{-2}$ CO molecules photon⁻¹. The error is estimated based on the results from two experiments performed under the same conditions.

As mentioned above, according to Öberg et al. (2007) the photodissociation rate of CO ice is constant as long as 1 ML is left on the surface. This result would imply that the photons absorbed deeper than 1 ML have no effect on the photodesorption. We find that the photodesorption rate does not depend on the ice thickness unless the ice thickness is less than about 5 ML of CO for experiments performed at 7 or 8 K, as shown in Fig. 13, which indicates that the photons absorbed deeper than 5 ML cannot transfer their energy to the top ML, and therefore do not lead to photodesorption. It is difficult to envisage how a single monolayer of CO ice can lead to the same photodesorption value as a thicker ice layer. The ideal case of a completely homogeneous distribution of molecules for 1 ML thickness is not attained in practice, at least not when the ice is formed using deposition tubes, as in the Öberg et al. (2007) experiments and our own experiments. Even if there was no contribution from the adjacent monolayers to the photodesorption of the top monolayer, which is actually not the case as Öberg et al. (2009) shows, an average thickness of 1 ML means that in some spots of the substrate the thickness is 2 or more molecules, while other spots are empty, with no CO molecules covering the substrate, thus not contributing to photodesorption. As a result, the expected photodesorption value for an average thickness of 1 ML should be lower than for thicker ices.

Below, we determine the quantum yield for CO photodesorption per absorbed UV photon. For that, the value of the UV absorption cross section of CO ice for the emission range of the hydrogen UV lamp used in our experiments, $\sigma[115\text{--}170\text{ nm}]$, is needed. This value is calculated in Appendix B. For 1 ML of CO ice, i.e. $N = 1 \times 10^{15}$ molecules cm⁻², and $\sigma[115\text{--}170\text{ nm}] \approx 3.8 \times 10^{-18}$ cm² per photon of average energy 9.2 eV, the fraction of UV photons absorbed is given by $(I_0[115\text{--}170\text{ nm}] - I[115\text{--}170\text{ nm}])/I_0[115\text{--}170\text{ nm}] = 1 - I[115\text{--}170\text{ nm}]/I_0[115\text{--}170\text{ nm}] = 1 - \exp(-\sigma[115\text{--}170\text{ nm}]N) \approx 0.0038$, i.e. 0.38% of the photons are absorbed, where I_0 is the incident photon flux and I the outgoing photon flux. Similarly, at the top 5 ML that were found to play a role in the photodesorption, 1.88% of the incident photons are absorbed. For an incident flux of 2.5×10^{14} photons cm⁻² s⁻¹ with average energy 9.2 eV we find that 4.7×10^{12} photons cm⁻² s⁻¹ are absorbed in the top 5 ML. Therefore, the quantum yield per absorbed photon in the top 5 ML, i.e. those involved in photodesorption, is 1.6×10^{13} molecules cm⁻² s⁻¹ / 4.7×10^{12} photons cm⁻² s⁻¹ ≈ 3.4 molecules photon⁻¹ for the 7 K experiment. For the 8 K experiment, the quantum yield is 1.3×10^{13} molecules cm⁻² s⁻¹ / 4.7×10^{12} photons cm⁻² s⁻¹ ≈ 2.8 molecules photon⁻¹.

In terms of CO photodesorption rates, our results can be summarized as follows. For ice thicknesses $x < 5$ ML, the photodesorption rate is expected to depend on the number of photons

absorbed as a function of the ice thickness, $(I_0 - I)$, for a given number x of monolayers, given by

$$\begin{aligned} R_{\text{ph-des}}(x < 5 \text{ ML}) &= (I_0 - I) \cdot QY = I_0 \cdot \left(1 - \frac{I}{I_0}\right) \cdot QY \\ &= I_0 \cdot \left(1 - e^{-\sigma N}\right) \cdot QY, \end{aligned} \quad (6)$$

in molecules cm⁻² s⁻¹, where $I_0 = 2.5 \times 10^{14}$ photons cm⁻² s⁻¹, the column density $N = x \times 10^{15}$ molecules cm⁻², and the quantum yield values at 7 and 8 K per absorbed photon in the top 5 ML were estimated above. We introduce a dimensionless parameter $k > 1$ to fit the datapoints of Fig. 13 when the ice thickness is below 5 ML. The $k > 1$ parameter multiplies the term $I/I_0 = e^{-\sigma N}$, thus increasing the fraction of outgoing photons, i.e. the fraction of photons absorbed in the ice is reduced by $k > 1$, effectively decreasing the photodesorption rate of Eq. (6). This parameter should be related to variations in the real ice thickness value throughout the surface of the substrate, substrate effects like the desorption of CO molecules from the KBr substrate surface where the ice was deposited rather than desorption of a CO molecule from CO ice, etc.; therefore,

$$R_{\text{ph-des}}(x < 5 \text{ ML}) = I_0 \cdot (1 - k \cdot e^{-\sigma N}) \cdot QY. \quad (7)$$

The k values that fit the datapoints in Fig. 13 for the 7 and 8 K experiments are 1.01 and 1.0035, respectively. For $x \geq 5$ ML, there is no dependence on the ice thickness and

$$R_{\text{ph-des}}(x \geq 5 \text{ ML}) = I_0 \cdot (1 - e^{-\sigma \cdot 5 \times 10^{15}}) \cdot QY. \quad (8)$$

It was suggested that a possible source of high vibrational excitation that should be linear in excitation current could be radiationless conversion of electronic to vibrational excitation, and coupling electronic to translational energy via radiationless decay could be an important channel for the electronically stimulated desorption from CO ice (Rakhovskaia et al. 1995). This might explain the linear dependence of photodesorption with radiation time observed by Öberg et al. (2007), which is confirmed by the data shown in Fig. 13. As suggested by Öberg et al. (2007), after UV absorption the excited molecule relaxes via a radiationless transition into vibrationally excited states of the electronic ground state, which subsequently transfer part of this intramolecular energy to the weak intermolecular bonds with neighboring CO molecules, resulting in a desorption event. This desorption event may consist of more than the originally excited molecule desorbing, which would explain that the quantum yield values per absorbed photon measured at 7 and 8 K were higher than unity, respectively 3.4 and 2.8 molecules per photon absorbed in the top 5 ML.

As we previously discussed, our results indicate that the top 5 ML are involved in the photodesorption. This can be explained if a fraction of the intramolecular energy of the excited CO molecule is transferred to the weak intermolecular bonds with neighboring CO molecules, as suggested by Öberg et al. (2007). Indeed, photodesorption of an N₂:CO ice mixture shows that about 5% of the UV photon absorptions of CO molecules result in the desorption of a neighboring molecule rather than the desorption of the originally excited molecule (Öberg et al. 2009), and the energy transfer between CO molecules should be much more efficient than between CO and N₂ molecules.

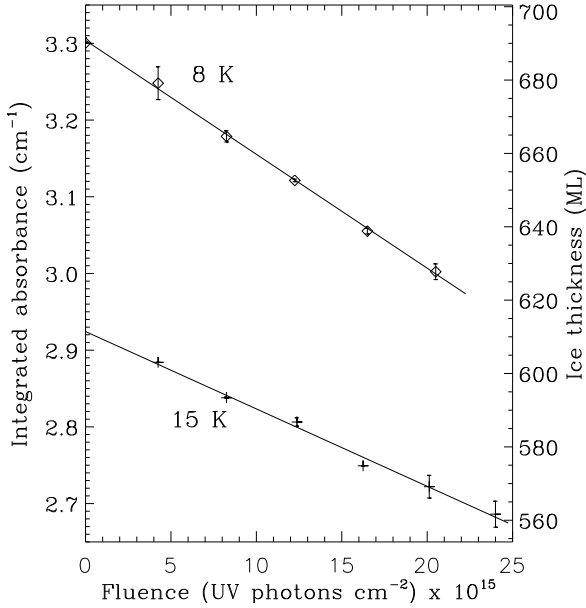


Fig. 15. Decrease in the absorption area (integrated absorbance) of the CO ice band as a function of fluence for two different ice temperatures, 8 K and 15 K, see Sect. 3 for determination of the integrated absorbance. Data points and errorbars result from the average of two experiments performed under the same conditions. Roughly, 1 ML of ice is equivalent to a column density of 1×10^{15} molecules cm^{-2} .

6.2. Photodesorption of thick CO ice at 8 K and 15 K

We performed photodesorption experiments of ices with thicknesses >600 ML at 8 K and 15 K and searched for possible products of irradiation. The values of the integrated absorbance as a function of fluence are shown in Fig. 15. A linear fit of the data provides the photodesorption rates of CO ice at 8 K and 15 K, 1.3×10^{13} CO molecules $\text{cm}^{-2} \text{s}^{-1}$ and 8.8×10^{12} CO molecules $\text{cm}^{-2} \text{s}^{-1}$, respectively. For the measured UV flux of 2.5×10^{14} photons $\text{cm}^{-2} \text{s}^{-1}$, these values correspond to photodesorption yields per incident photon of $5.4 \pm 0.5 \times 10^{-2}$ CO molecules photon^{-1} at 8 K and $3.5 \pm 0.5 \times 10^{-2}$ CO molecules photon^{-1} at 15 K. This result confirms the decrease in the photodesorption yield as the CO ice temperature increases observed by Öberg et al. (2007). Our CO photodesorption yield measured at 15 K is about 10 times higher than estimated by Öberg et al. (2007) at the same temperature. Experiments performed by us with a flux similar to the one used by Öberg et al. (2007), obtained removing the quartz tube that is placed between the UV lamp and the substrate, showed that the CO photodesorption rate decreased linearly with flux, a five times lower flux leads to a five times lower CO photodesorption rate, but the value of the CO photodesorption yield is independent of the flux value. A possible explanation of such a difference is that reflection absorption infrared spectroscopy (RAIRS) used by Öberg et al. (2007) does not provide a direct measurement of the ice absorbance, and calibration was required. The transmittance FTIR spectroscopy used in our experiments provides a direct measurement of the ice absorbance, which converts to the number of molecules photodesorbed.

The photodesorption yields given above are in fact estimated by measuring the decrease in the infrared absorption of CO during UV irradiation. The formation of photoproducts may also contribute to the observed decrease of the CO abundance. Öberg et al. (2007) find that less than 0.2% of the CO ice is converted to CO_2 after 8 h of irradiation of 8 ML CO ice. Our experiments on the irradiation of thin ices reported in Sect. 6.1 support this

result. The infrared bands of photoproducts were only clearly detected in the thick CO ice photodesorption experiments reported here. They are associated to CO_2 , C_3O , and C_3O_2 , which were previously detected in CO irradiation experiments (Gerakines et al. 1996, and references therein; Gerakines & Moore 2001; Loeffler et al. 2005). These photoproducts account for less than 5% of the CO band decrease in our experiments, $\text{CO}_2 \leq 3\%$. Our results agree with those obtained by Loeffler et al. (2005). Our data, not shown, is similar to those represented in Fig. 2 of that publication, which shows that the amount of CO_2 formed is about 2% with respect to the initial CO. Since CO is the main photoproduct of CO_2 ice irradiation (Gerakines et al. 1996), further irradiation of the CO_2 can reform the CO. Therefore, the decrease of the CO ice column density observed by means of FTIR is mainly due to the photodesorption of CO, and, in comparison, the formation of photoproducts is a minor effect.

7. Astrophysical implications

In the cold interiors of dark molecular clouds, most molecules are expected to stick to grains, thereby leading to depletion in the gas phase. CO was expected to deplete onto grains at temperatures below 20 K, but it is observed in the gas phase in cold clouds like L183, provided that the density is below $\approx 3 \times 10^4 \text{ cm}^{-3}$ (Pagani et al. 2005, and references therein). Tafalla et al. (2004) find 2.5 and $7.8 \times 10^4 \text{ cm}^{-3}$ for the minimum densities required for depletion of CO gas. In addition to these works on the study of photodesorption, others have explored the possibility of CO desorption induced by cosmic rays, which can play an important role inside dense clouds (Seperuelo Duarte et al. 2010, and references therein). The CO ice absorption profile near 2140 cm^{-1} shows that it can be embedded in a nearly pure separate ice phase (Ehrenfreund et al. 1996). In a H_2O -dominated ice matrix, the desorption of CO differs greatly from that of pure CO ice, and the results reported here are not applicable.

The rates of accretion $R_{\text{acc}}(\text{CO})$, thermal desorption $R_{\text{th-des}}(\text{CO})$, and photodesorption $R_{\text{ph-des}}(\text{CO})$ are computed as a function of time using a simple model of a quiescent dark cloud interior, where no processing by external UV flux occurs, and the UV photon flux induced by cosmic rays, $F \sim 1 \times 10^4$ photons $\text{cm}^{-2} \text{s}^{-1}$, dominates direct cosmic-ray desorption (Shen et al. 2004). The initial parameters of the cloud, unless otherwise specified, are the following: $T_{\text{gas}} = T_{\text{dust}} = 7 \text{ K}$ are the gas and dust temperatures, $n_{\text{H}} = 1.0\text{--}3 \times 10^4 \text{ cm}^{-3}$ and $n_{\text{CO}} = 9.5 \times 10^{-5} \times n_{\text{H}}$ (Frerking et al. 1982) are the densities of H and CO. We assume that all the CO molecules are initially in the gas phase. The masses of H and CO in grams are m_{H} and m_{CO} , and $m_{\text{CO}}(\text{amu}) = 28$ is the mass of CO in amu. We assume a density of $n_{\text{dust}} = \frac{0.01 \cdot n_{\text{H}} \cdot m_{\text{H}}}{1.33 \cdot \pi \cdot \rho \cdot r^3} = 1.33 \times 10^{-12} \cdot n_{\text{H}}$ dust grains with a constant radius, $r = 0.05 \times 10^{-4} \text{ cm}$ and density $\rho = 3 \text{ g cm}^{-3}$ (silicate core density). The sticking probability at 7–10 K is assumed to be unity, $f = 1$.

The accretion rate of CO molecules onto grains is given by

$$R_{\text{acc}}(\text{CO}) = n_{\text{g}}(\text{CO}) \cdot n_{\text{dust}} \cdot \pi \cdot r^2 \cdot \sqrt{\frac{3 \cdot k \cdot T_{\text{gas}}}{m_{\text{CO}}}} \cdot f \quad (9)$$

in molecules $\text{cm}^{-3} \text{s}^{-1}$, where k is the Boltzmann constant. For ice thicknesses $x = \frac{n_{\text{s}}(\text{CO})(t)}{10^{15} \cdot n_{\text{dust}} \cdot 4 \cdot \pi \cdot r^2} < 5 \text{ ML}$, where $n_{\text{s}}(\text{CO})(t) = n_{\text{g}}(\text{CO})(0) - n_{\text{g}}(\text{CO})(t)$, the photodesorption rate can be expressed as

$$R_{\text{ph-des}}(x < 5 \text{ ML})(\text{CO}) = F \cdot (1 - k \cdot e^{-\sigma N}) \cdot QY \cdot n_{\text{dust}} \cdot \pi \cdot r^2, \quad (10)$$

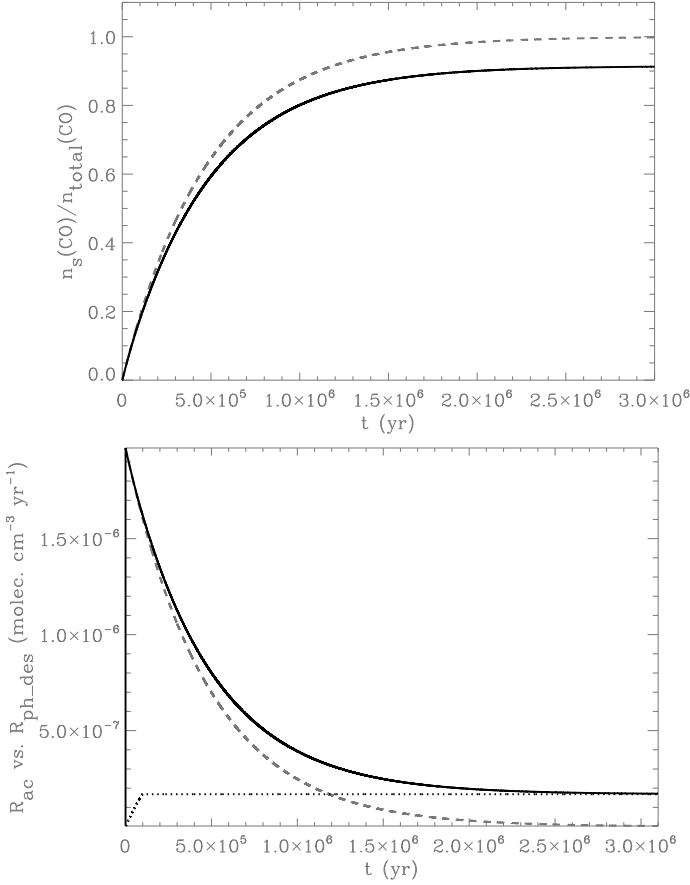


Fig. 16. *Top panel:* formation of CO ice mantles as a function of the cloud lifetime for a cloud density of $1 \times 10^4 \text{ cm}^{-3}$ and $T_{\text{gas}} = T_{\text{dust}} = 7 \text{ K}$, with no photodesorption (dashed gray trace) and if photodesorption balances the accretion (solid black trace). *Bottom panel:* $R_{\text{acc}}(\text{CO})$ if there is no photodesorption (dashed gray trace), $R_{\text{acc}}(\text{CO})$ if photodesorption balances the accretion (solid black trace), and $R_{\text{ph-des}}(\text{CO})$ represented as a dotted trace for the same initial parameters as a function of the cloud lifetime.

in $\text{molecules cm}^{-3} \text{ s}^{-1}$, where we use the parameter values from Sect. 6.1, and for $x \geq 5 \text{ ML}$

$$R_{\text{ph-des}}(x \geq 5 \text{ ML})(\text{CO}) = F \cdot (1 - e^{-\sigma v \times 10^{15}}) \cdot QY \cdot n_{\text{dust}} \cdot \pi \cdot r^2, \quad (11)$$

in $\text{molecules cm}^{-3} \text{ s}^{-1}$, entering the parameter values from Sect. 6.1. The thermal desorption of CO is

$$R_{\text{th-des}}(\text{CO}) = \left(\nu_0(\text{H}_2 \text{ ind. CO}) \cdot \exp\left(-\frac{E_d(\text{H}_2 \text{ ind. CO})}{T_{\text{dust}}}\right) + \nu_0(\text{CO}) \cdot \exp\left(-\frac{E_d(\text{CO})}{T_{\text{dust}}}\right) \right) \cdot n_{\text{dust}} \cdot 4 \cdot \pi \cdot r^2 \quad (12)$$

in $\text{molecules cm}^{-3} \text{ s}^{-1}$, with $\nu_0(\text{H}_2 \text{ ind. CO}) = 5.1 \times 10^{21} \text{ molecules cm}^{-2} \text{ s}^{-1}$, $\nu_0(\text{CO}) = 6.5 \times 10^{26} \text{ molecules cm}^{-2} \text{ s}^{-1}$, $E_d(\text{H}_2 \text{ ind. CO}) = 490 \text{ K}$, $E_d(\text{CO}) = 834 \text{ K}$ from Sect. 5. The rate of ice mantle build-up is

$$\frac{dn_s(\text{CO})}{dt} = R_{\text{acc}}(\text{CO}) - R_{\text{ph-des}}(\text{CO}) - R_{\text{th-des}}(\text{CO}). \quad (13)$$

At temperatures below 10 K, $R_{\text{th-des}}(\text{CO}) = 0$ and $R_{\text{ph-des}}(\text{CO})$ drive the desorption. The top panel of Fig. 16 shows the formation of CO ice mantles as a function of the cloud lifetime,

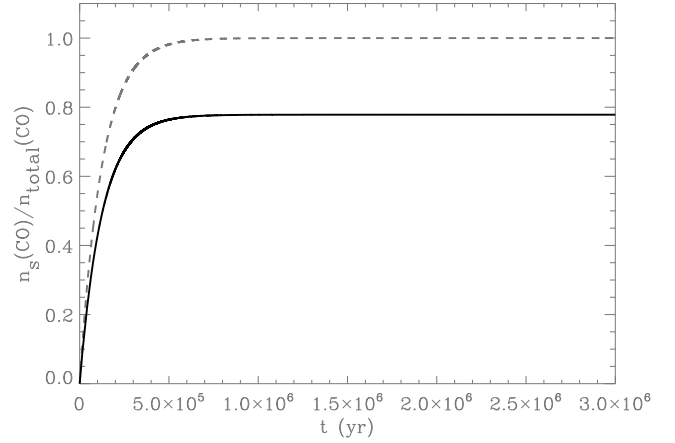


Fig. 17. CO ice mantle build up as a function of the cloud lifetime, expressed as $\frac{n_s(\text{CO})}{n_{\text{total}}(\text{CO})}$, for a cloud density of $3 \times 10^4 \text{ cm}^{-3}$ and $T_{\text{gas}} = T_{\text{dust}} = 11.5 \text{ K}$. The dashed gray trace corresponds to accretion for $R_{\text{th-des}}(\text{CO}) = 0$. The solid black trace corresponds to Eq. (13) with $R_{\text{ph-des}}(\text{CO}) = 0$ and $R_{\text{th-des}}(\text{CO})$ from Eq. (12).

expressed as $\frac{n_s(\text{CO})}{n_{\text{total}}(\text{CO})}$, for a cloud density of $1 \times 10^4 \text{ cm}^{-3}$ and $T_{\text{gas}} = T_{\text{dust}} = 7 \text{ K}$. Simple accretion with no photodesorption, i.e. $R_{\text{ph-des}}(\text{CO}) = 0$, is shown. The curve corresponding to Eq. (13) with $R_{\text{ph-des}}(\text{CO})$ from Eqs. 7 and 8, and $R_{\text{th-des}}(\text{CO}) = 0$, i.e. no thermal desorption at 7 K is also represented. The time evolution of $R_{\text{acc}}(\text{CO})$ and $R_{\text{ph-des}}(\text{CO})$ is represented in the bottom panel of Fig. 16 for the same initial parameters. As expected from Eq. (8), the $R_{\text{ph-des}}(\text{CO})$ value is constant for ice mantle thicknesses $x \geq 5 \text{ ML}$. It is observed that, if photodesorption occurs, $\frac{n_s(\text{CO})}{n_{\text{total}}(\text{CO})} = 0.91$ after $t = 2.5 \times 10^6 \text{ yr}$. For a density of $1.5 \times 10^5 \text{ cm}^{-3}$, $\frac{n_s(\text{CO})}{n_{\text{total}}(\text{CO})} = 1$ (total gas depletion) after $t = 2 \times 10^5 \text{ yr}$. If the density is $3 \times 10^4 \text{ cm}^{-3}$, $\frac{n_s(\text{CO})}{n_{\text{total}}(\text{CO})} = 0.97$ after $t = 1 \times 10^6 \text{ yr}$. These values agree with the observed depletion of CO gas at those densities (Pagani et al. 2004, and references therein), mentioned above.

Figure 17 shows the CO ice mantle build up as a function of the cloud lifetime, expressed as $\frac{n_s(\text{CO})}{n_{\text{total}}(\text{CO})}$ for a cloud density of $3 \times 10^4 \text{ cm}^{-3}$ and $T_{\text{gas}} = T_{\text{dust}} = 11.5 \text{ K}$. Simple accretion in the absence of thermal desorption is shown, i.e. $R_{\text{th-des}}(\text{CO}) = 0$. The curve corresponding to Eq. (13) with $R_{\text{ph-des}}(\text{CO}) = 0$ and $R_{\text{th-des}}(\text{CO})$ from Eq. (12) is also represented. It is found that $\frac{n_s(\text{CO})}{n_{\text{total}}(\text{CO})} = 0.78$ after $t = 7.0 \times 10^5 \text{ yr}$. In fact, $\frac{n_s(\text{CO})}{n_{\text{total}}(\text{CO})} < 1$ at equilibrium after $t = 7.0 \times 10^5 \text{ yr}$ if $T_{\text{dust}} = T_{\text{gas}} \geq 11 \text{ K}$ for a cloud density of $3 \times 10^4 \text{ cm}^{-3}$. If only the usual CO ice desorption is taken into account with no contribution of H₂ induced CO ice desorption, as is usually the case in the literature, for density $3 \times 10^4 \text{ cm}^{-3}$, $\frac{n_s(\text{CO})}{n_{\text{total}}(\text{CO})} < 1$ after $t = 7 \times 10^5 \text{ yr}$ and $T_{\text{dust}} = T_{\text{gas}} \geq 14.5 \text{ K}$. Therefore, for the same density of a cloud, thermal desorption starts at 11 K if we consider H₂ induced CO ice desorption, and is not triggered until 14.5 K are reached if only the common CO desorption is considered.

8. Conclusions

The data reported here indicate that ISAC is performing as expected: base pressure down to $2.5 \times 10^{-11} \text{ mbar}$, a controlled substrate temperature from 7 K to 400 K, a deposition system for the preparation of complex gas mixtures, containing H₂O and CH₃OH vapors, and gas components such as CO, CO₂, and

CH₄, which is unique compared to other set-ups dedicated to astrochemistry. In addition, the CO experiments proved the utility of the in situ transmittance FTIR and QMS measurements for the performance of TPD experiments.

Based on the QMS measurements performed during TPD experiments, we observed that thermal desorption of CO ice driven by H₂ release from the ice starts at 15 K. As commonly observed, the peak in the desorption of CO occurs at 28 K. To our knowledge, we provide the first determination of the binding energy for CO desorption induced by the release of H₂ from the CO ice, 490 K. Since H₂ is abundant in dense cloud interiors, including a second term in the Polanyi-Wigner equation is justified in that astrophysical case. Our estimate of the binding energy of CO, 834 K, agrees with literature values: e.g. Acharyya et al. (2007) report 858 ± 15 K from similar experiments, and Pontoppidan (2006) obtained 814 ± 30 K from astrophysical observations.

The photodesorption yields of CO ice per incident photon at 7, 8, and 15 K, were respectively $6.4 \pm 0.5 \times 10^{-2}$, $5.4 \pm 0.5 \times 10^{-2}$, and $3.5 \pm 0.5 \times 10^{-2}$ CO molecules photon ($7.3\text{--}10.5$ eV)⁻¹. This estimation of the photodesorption yield at 15 K is about 10 times higher than estimated by Öberg et al. (2007) at the same temperature. We showed that the top 5 ML are involved in the UV-photodesorption of CO ice at 7 K and 8 K, which requires that a fraction of the intramolecular energy of the photon-excited molecule is transferred to the weak intermolecular bonds with neighboring CO molecules. We estimated the UV absorption cross section of CO ice from its UV absorption spectrum published in the literature corresponding to the emission range of our UV lamp, see Appendix B. That allowed determination of the quantum yield of photodesorption per absorbed photon in the top 5 ML that play a role in photodesorption: for the 7 and 8 K experiments, 3.4 and 2.8 molecules photon ($7.3\text{--}10.5$ eV)⁻¹, respectively.

Our simple model of a quiescent cloud interior suggests that photodesorption can explain the observations of CO in the gas phase for densities below $3\text{--}7 \times 10^4$ cm⁻³ (Pagani et al. 2005, and references therein). For the same density of a cloud, 3×10^4 cm⁻³, thermal desorption starts at $T = 11$ K if we consider CO desorption induced by the release of H₂ from the CO ice, and is not triggered until $T = 14.5$ K is reached if only the usual CO desorption is considered. This has strong implications for CO ice mantle build up.

Acknowledgements. We thank Profs. J. F. Ogilvie, B.-M. Cheng, and C.-Y. R. Wu for their support on calculating the UV absorption cross section of CO. We acknowledge E. Dartois, W.-F. Thi, and M. P. Zorzano for discussions. We are grateful to the former director of the CAB, Prof. J. Pérez Mercader, for his support on this project. A.J.E. is supported by a research training grant from INTA. G.M.M.C. was financed by a Ramón y Cajal research contract from the MCYT in Spain. This work was supported by project AYA2008-06374 funded by Spanish MICINN.

Appendix A: Determination of the UV lamp flux

To estimate the flux of the UV lamp we used the expression

$$QE = \frac{N(t) - N(0)}{I_0 \cdot t} \quad (14)$$

where QE is the quantum efficiency (molecules photon⁻¹) for the formation of the photoproduct in the ice, $N(0)$ and $N(t)$ the ice column densities of the photoproduct prior to irradiation and after irradiation time t , and I_0 is the incident photon flux at the sample position. We deposited and irradiated an O₂ ice layer of more than 300 nm thickness at 8 K under the same conditions

as the CO photodesorption experiments. The column densities of the O₃ photoproduct were calculated using Eq. (1) adopting a band strength value of $A(\text{O}_3) = 1.4 \times 10^{-17}$ cm molecule⁻¹ and $QE = 1.92$ (Cottin et al. 2003, and references therein). The flux estimate derived from Eq. (14) is $I_0 \approx 2.6 \times 10^{14}$ photons cm⁻² s⁻¹. Also, CO formation from CO₂ ice photolysis experiments with $A(\text{CO}) = 1.1 \times 10^{-17}$ cm molecule⁻¹ and $QE = 1.0$ (Cottin et al. 2000, and references therein) was used to measure the UV flux of the lamp, giving a similar result, $I_0 \approx 2.5 \times 10^{14}$ photons cm⁻² s⁻¹.

Appendix B: Calculation of UV absorption cross section of solid CO

A direct value of the UV absorption cross section of CO ice in the wavelength range of the hydrogen UV lamp has to our knowledge not been reported. et al. (2005) measured the first UV absorption spectrum of CO ice, deposited at 10 K and a 7.4 nmol s⁻¹ deposition rate, i.e. ~ 4.5 ML s⁻¹. The UV absorption cross section corresponding to the 115–170 nm wavelength range ($86956.5\text{--}58823.5$ cm⁻¹ in wavenumbers) of the hydrogen UV lamp can be obtained from the UV absorption spectrum as follows. The photon flux, $I[k_1, k_2]$, through the solid with the integration performed over the wavenumber interval $[k_1, k_2]$ in cm⁻¹, is given by the Lambert-Beer law,

$$\begin{aligned} I[k_1, k_2] &= \int_{k_1}^{k_2} I_0(k) \exp(-n l \sigma(k)) dk \\ &= \int_{k_1}^{k_2} I_0(k) \exp(-\tau(k)) dk \end{aligned} \quad (15)$$

where $I_0(k)$ is the initial photon flux, n the concentration of the absorbers that can be expressed in molecules cm⁻³, l the pathlength of the photons through the material, $\sigma(k)$ the absorption cross section in cm⁻², and $\tau(k)$ the optical depth. The UV absorption cross section over the $[k_1, k_2]$ range is defined as

$$\sigma[k_1, k_2] = \frac{1}{n l} \int_{k_1}^{k_2} \tau(k) dk = \frac{2.303}{N} \int_{k_1}^{k_2} A(k) dk \quad (16)$$

where $N = n \cdot l$ is the column density and the absorbance, $A(k)$, corresponds to $A(k) = \log_{10} \left(\frac{I_0(k)}{I(k)} \right) = (1/2.303) \ln \left(\frac{I_0(k)}{I(k)} \right) = (1/2.303) \cdot \tau(k)$.

We use the results from Lu et al. (2005) to estimate $\sigma[k_1, k_2]$ for solid CO in the $[k_1, k_2] = [86956.5\text{--}58823.5$ cm⁻¹] range. The absorption spectrum of solid CO is given in Fig. 2 of Lu et al. (2005) at $T = 10$ K, a rate of deposition of 7.4 nmol s⁻¹ during 90 s, resolution 0.03 nm, and scan step 0.1 nm. The diameter of the substrate for CO deposition was 25 mm (Cheng, private communication). Therefore, the value of the CO ice column density was $N = 8.2 \times 10^{16}$ molecules cm⁻². Again, only the bands associated to transitions to electronic states A¹Π are considered since other transitions do not fall in the emission range of our hydrogen UV lamp, with an integrated absorbance value as a function of k (cm⁻¹) of $A[86956.5\text{--}58823.5$ cm⁻¹] ~ 10055 , obtained from Table 2 of Lu et al. (2005). From Eq. (16) we obtain $\sigma[86956.5\text{--}58823.5$ cm⁻¹] = 2.8×10^{-13} cm² cm⁻¹, which coincides with the 115–170 nm wavelength range. If, instead of wavenumbers, k in cm⁻¹, the absorbance is represented in the photon-energy E scale in eV, then $k = \lambda^{-1} = \frac{E}{hc}$ and $dk = -\frac{d\lambda}{\lambda^2} = \frac{dE}{hc}$ with $hc = 1.24 \times 10^{-4}$ eV cm, so that

$$1.24 \times 10^{-4} \cdot \sigma[k_1, k_2] \text{ cm}^2 \text{ cm}^{-1} = \sigma[E_1, E_2] \text{ cm}^2 \text{ eV}. \quad (17)$$

Using Eq. (17) we have $\sigma[86956.5\text{--}58823.5\text{ cm}^{-1}] = 2.8 \times 10^{-13}\text{ cm}^2\text{ cm}^{-1} = 3.5 \times 10^{-17}\text{ cm}^2\text{ eV}$ for the 115–170 nm range. For our lamp, we estimated that the average photon energy in the 115–170 nm wavelength range is 9.2 eV. Therefore $\sigma[86956.5\text{--}58823.5\text{ cm}^{-1}] = \sigma[115\text{--}170\text{ nm}] \approx 3.8 \times 10^{-18}\text{ cm}^2\text{ per photon of average energy 9.2 eV}$. This value is not very different from the value obtained by Loeffler et al. (2005) for Lyman- α photons of 10.2 eV (121.6 nm), $2.6 \times 10^{-18}\text{ cm}^2\text{ per 10.2 eV photon}$.

References

- Acharyya, K., Fuchs, G. W., Fraser, H. J., van Dishoeck, E. F., & Linnartz, H. 2007, A&A, 466, 1005
- Bisschop, S. E., Fraser, H. J., Öberg, K. I., van Dishoeck, E. F., & Schlemmer, S. 2006, A&A, 449, 1297
- Collings, M. P., Anderson, M. A., Chem, R., et al. 2004, MNRAS, 354, 1133
- Cottin, H., Gazeau, M.-C., Doussin, J.-F., & Raulin, F. 2000, J. Photochem. Photobio. A, 135, 53
- Cottin, H., Moore, M. H., & Bénilan, Y. 2003, ApJ, 590, 874
- Dartois, E. 2006, A&A, 445, 959
- Ehrenfreund, P., Boogert, A. C. A., Gerakines, P. A., et al. 1996, A&A, 315, L341
- Frerking, M. A., Langer, W. D., & Wilson, R. W. 1982, ApJ, 262, 590
- Gerakines, P. A., & Moore, M. H. 2001, Icarus, 154, 372
- Gerakines, P. A., Schutte, W. A., & Ehrenfreund, P. 1996, A&A, 312, 289
- Gibb, E. L., Whittet, D. C. B., & Chiar, J. E. 2001, ApJ, 558, 702
- Jenniskens, P., Baratta, G. A., Kouchi, A., et al. 1993, A&A, 273, 583
- Jiang, G. J., Person, W. B., & Brown, K. G. 1975, J. Chem. Phys., 64, 1201
- Kouchi, A. 1990, J. Cryst. Growth, 99, 1220
- Loeffler, M. J., Baratta, G. A., Palumbo, M. E., Strazzulla, G., & Baragiola, R. A. 2005, A&A, 435, 587
- Lu, H.-C., Chen, H.-K., Cheng, B.-M., Kuo, Y.-P., & Ogilvie, J. F. 2005, J. Phys. B: At. Mol. Opt. Phys., 38, 3693
- Muñoz Caro, G. M., & Schutte, W. A. 2003, A&A, 412, 121
- Öberg, K. I., Fuchs, G. W., Awad, Z., et al. 2007, ApJ, 662, L23
- Öberg, K. I., van Dishoeck, E. F., & Linnartz, H. 2009, A&A, 496, 281
- Pagani, L., Pardo, J.-R., Apponi, A. J., Bacmann, A., & Cabrit, S. 2005, A&A, 429, 181
- Palumbo, M. E., & Strazzulla, G. 1993, A&A, 269, 568
- Palumbo, M. E., Baratta, G. A., Collings, M. P., & McCoustra, M. R. S. 2006, Phys. Chem. Chem. Phys., 8, 279
- Pontoppidan, K. M. 2006, A&A, 453, L47
- Pontoppidan, K. M., Dullemond, C. P., van Dishoeck, E. F., et al. 2005, ApJ, 622, 463
- Rakhovskaia, O., Wiethoff, P., & Feulner, P. 1995, NIM B, 101, 169
- Rowland, B., Fisher, M., & Devlin, J. P. 1991, J. Chem. Phys., 95, 1378
- Sandford, S. A., & Allamandola, L. J. 1988, Icarus, 76, 201
- Sandford, S. A., Allamandola, L. J., Tielens, A. G. G. M., & Valero, G. J. 1988, ApJ, 329, 498
- Seperuelo Duarte, E., Domaracka, A., Boduch, P., et al. 2010, A&A, 512, A71
- Shen, C. J., Greenberg, J. M., Schutte, W. A., & van Dishoeck, E. F. 2004, A&A, 415, 203
- Tafalla, M., Myers, P. C., Caselli, P., & Walmsley, C. M. 2004, A&A, 416, 191
- Thi, W. F., Pontoppidan, K. M., van Dishoeck, E. F., Dartois, E., & d'Hendecourt, L. 2002, A&A, 394, L27
- Weber, P., & Greenberg, J. M. 1985, Nature, 316, 403